NANO LETTERS
Letter
Cite This: Nano Lett. 2019, 19, 2037−2043
pubs.acs.org/NanoLett

Operando Investigation into Dynamic Evolution of Cathode−Electrolyte Interfaces in a Li-Ion Battery

Dongchang Chen,[†,‡] Mahmoud A. Mahmoud,[‡,∥] Jeng-Han Wang,[§] Gordon H. Waller,[†] Bote Zhao,[†] Chong Qu,[†] Mostafa A. El-Sayed,[‡] and Meilin Liu*[,†]

[†]School of Materials Science and Engineering, Center for Innovative Fuel Cell and Battery Technologies, Georgia Institute of Technology, 771 Ferst Drive, Atlanta, Georgia 30332-0245, United States

[‡]Laser Dynamics Laboratory, School of Chemistry and Biochemistry, Georgia Institute of Technology, 901 Atlantic Drive, Atlanta, Georgia 30332-0400, United States

[§]Department of Chemistry, National Taiwan Normal University, 88, Sec. 4 Ting-Zhou Road, Taipei 11677, Taiwan R.O.C

[∥]Chemical Engineering, Department of Biomedical Engineering, College of Engineering, The University of Texas at San Antonio, One UTSA Circle, San Antonio, Texas 78249, United States

Supporting Information

ABSTRACT: While Li-ion battery cathode−electrolyte interfaces (CEIs) have been extensively investigated in recent decades, accurately identifying the chemical nature and tracking the dynamics of the CEIs during electrochemical cycling still remain a grand challenge. Here we report our findings in the investigation into the dynamic evolution of the interface between a $LiNi_{0.33}Co_{0.33}Mn_{0.33}O_2$ (LNMC) cathode and an ethylene carbonate/dimethyl carbonate (EC/DMC)-based electrolyte using surface-enhanced Raman spectroscopy (SERS) performed on a model cell under typical battery operating conditions. In particular, the strong SERS activity provided by a monolayer of Au nanocubes deposited on a model LNMC electrode (additive-free) enables quasi-quantitative assessment of the CEI evolution during cycling, proving information vital to revealing the dynamics of the species adsorbed on the LNMC surface as a function of cell potential. Furthermore, our theoretical calculation, which is based on the interaction between a model interface-bound molecule and a model LNMC surface, agrees with our experimental observation. The carefully designed operando SERS platform has demonstrated high sensitivity, good surface specificity, and excellent compatibility with extensive electrochemical measurements; it is also applicable to fundamental studies of dynamic interfaces in other electrochemical energy storage and conversion systems.

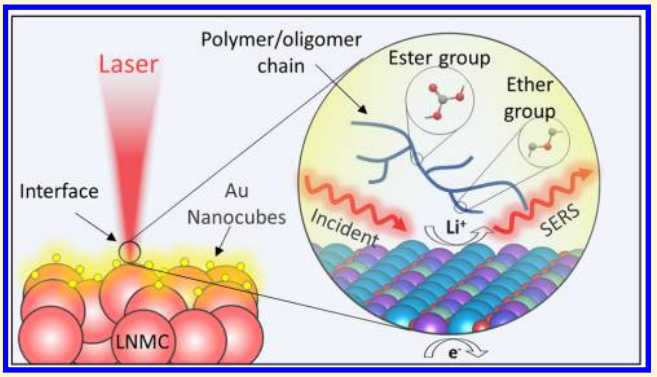

KEYWORDS: *Raman spectroscopy, surface-enhanced Raman spectroscopy (SERS), cathode−electrolyte interface (CEI), lithium-ion battery*

In modern energy storage industry, Li-ion batteries undoubtedly play an irreplaceable role because of their unparalleled advantages over other types of batteries.[1−3] The performance of a Li-ion battery depends sensitively on the electrochemical behavior of the electrode−electrolyte interfaces, including obtainable energy density, rate capability, cycling stability, and operational life.[4−10] Understanding the nature of the interfaces is imperative to battery performance optimization via rationally tailoring the interface. The difficulty in understanding the electrode−electrolyte interfaces is related to the chemical compatibility between the electrode and the electrolyte.[4] For instance, an ethylene carbonate/dimethyl carbonate (EC/DMC)-based electrolyte will react directly with the anode when its potential is below 1.0 V (vs Li^+/Li) or the cathode when its potential is above 5.0 V (vs Li^+/Li), producing an obvious solid electrolyte interphase (SEI) or other byproducts.[4,11,12] Such an easily detectable interphase formed between an electrode and an electrolyte has been extensively studied using various analytical techniques to unravel the mechanism of the interfacial reactions.[4] However, most Li-ion battery cathode−electrolyte interfaces are thermodynamically stable.[4] For example, many successful cathode materials, including $Li(NiCoMn)O_2$ (LNMC), $LiCoO_2$, $LiMn_2O_4$, and $LiFePO_4$, are typically operated within the stability window of Li-ion battery electrolytes.[11,13,14] For a thermodynamically stable cathode−electrolyte interface, there is little direct reaction between the electrode and the electrolyte, and the amount of the species adsorbed on

Received: January 15, 2019
Revised: February 20, 2019
Published: February 25, 2019

DOI: 10.1021/acs.nanolett.9b00179
Nano Lett. 2019, 19, 2037−2043

electrode surfaces is very limited,[4] in contrast to easily detectable solid electrolyte interphases for anodes. The tiny amount of interfacial species that define the cathode−electrolyte interface poses a great challenge to accurately investigate the CEI chemistry. Yet, the performance of a battery is strongly correlated to the electrochemical behavior of these interfaces.[15] Thus, understanding of the behavior of these interfaces is crucial to further optimization of battery performances. More importantly, the composition of the CEIs may change with electrochemical testing conditions. Identifying interfacial chemical species and quantifying their evolution under in situ/operando conditions require chemical fingerprinting techniques with both high specificity and high sensitivity applied to real interfaces subject to electrochemical operation. To date, unfortunately, most studies of interfaces were performed under ex situ or nonoperando conditions; the dynamic evolutions of CEIs during battery cycling are yet to be fully understood.[4,5]

The key to realize fast and reliable investigation of interfacial dynamics is to develop a well-designed reliable characterization system. Vibrational spectroscopy is a very powerful tool to identify chemical species from their characteristic vibrational modes and mode energies.[4,6,16−20] Comparing to Infrared spectroscopy, Raman spectroscopy is ideally suited for in situ/operando battery platforms,[16,21] by avoiding massive infrared absorption of electrolyte solvents. More importantly, when combined with carefully designed plasmonic materials, such as Au and Ag nanoparticles, plasmonic resonance with incident Raman laser enables surface-enhanced Raman spectroscopy (SERS).[22,23] Combining SERS with in situ/operando platforms would enable fast and reliable chemical fingerprinting for complicated systems.[16,24] In recent years, in situ/operando SERS techniques have been successfully applied to characterization of thermodynamically unstable Li-ion battery interfaces.[25,26] In these studies, assembly of SERS nanoparticles was not emphasized, because the amount of interfacial products resulted from the reactions between the electrode and the electrolyte is plenty for easy identification. However, for studies of a thermodynamically stable CEI, a monolayer assembly of SERS-active nanoparticles must be carefully designed, rather than randomly distributed or aggregated particle groups, in order to authentically and most effectively track the dynamic evolution of the CEI, because the amount of the associated interfacial species is very small and difficult to detect. In this work, we applied operando SERS to the investigation into the dynamic evolution of the CEI for an LNMC electrode, which is one of the most promising cathode materials. Au nanocubes, which feature excellent SERS activity, were deposited as a monolayer on a binder-free LNMC electrode surface. Raman scattering was greatly enhanced, providing excellent sensitivity to the changes in vibration modes of the chemical species generated on the surface of the LNMC electrode in an EC/DMC-based electrolyte under operating conditions. By analyzing the evolution of the spectral features during consecutive cell cycling, we found that ether and ester species were favorably formed on the surface of the LNMC electrode at lower potential. Additionally, we proposed a model CEI that contains ester and ether functional groups and a LNMC surface to simulate the behavior of the interface. The calculated evolution of the model CEI agrees well with our experimental observations.

A model LNMC electrode (binder free) was fabricated using LNMC powders derived from a sol−gel process (Supporting Information). The particle size varied from 200 to 400 nm, as seen from the scanning electron microscope (SEM) image shown in Figure 1a and the phase purity was confirmed by X-ray diffraction (XRD, Figure 1b). Rietveld refinement confirms that the LNMC crystallizes in a layered structure ($R\bar{3}m$) and the structural parameters (i.e., lattice constants, Li, and transition metal sites) are consistent with those reported in previous studies.[27] To enhance the Raman scattering from the interfaces, we select Au nanocubes as the SERS-active nanoparticles, which are well suited for operando measurements in electrochemical cells because they possess strong enhancement capability and are more chemically inert than Ag nanoparticles.[28] In order to dramatically enhance the sensitivity and specificity to the chemical species on the LNMC CEI, Au nanocubes are further assembled to a monolayer on the electrode surface via the Langmuir−Blodgett method.[29,30] Monolayer deposition was first confirmed on Si wafer. The Au nanocubes have an accurately controlled size (Figure 1c, ∼40 nm) and the assembly displays a well-

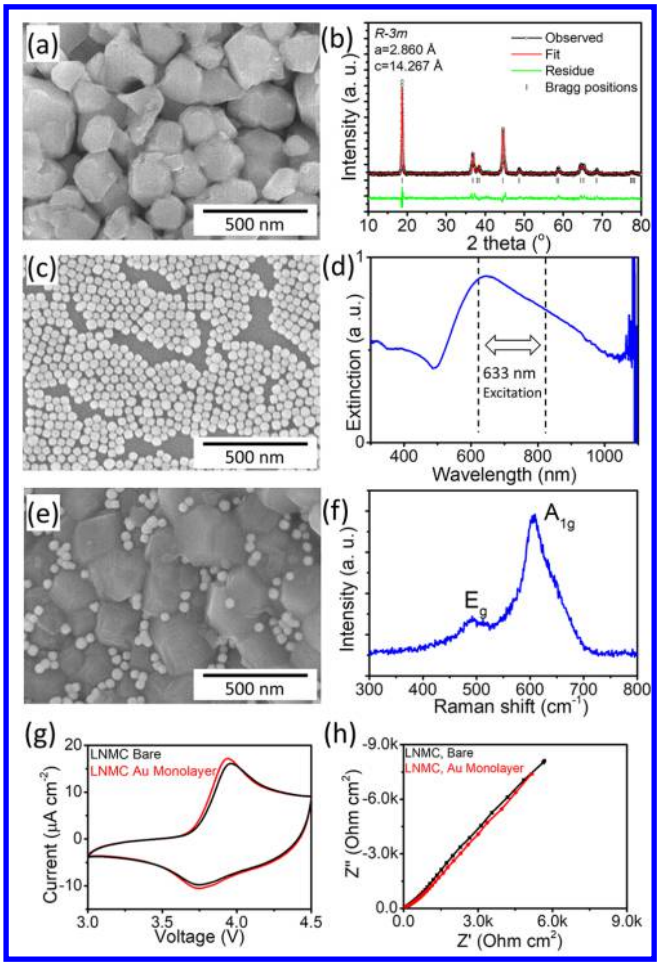

Figure 1. (a) SEM image and (b) X-ray diffraction and the corresponding Rietveld refinement of the LNMC powders derived from a sol−gel process. (c) A monolayer of Au nanocubes assembly deposited on a Si wafer via the Langmuir−Blodgett method. (d) Extinction spectrum of a monolayer of Au nanocubes assembly, showing its LSPR profile. (e) SEM image and (f) Raman spectrum of a LNMC model electrode with deposited Au nanocube via the Langmuir−Blodgett method. (g) CV profiles and (h) Nyquist plots of impedance spectra of model LNMC electrodes with and without Au nanocube deposition.

DOI: 10.1021/acs.nanolett.9b00179
Nano Lett. 2019, 19, 2037−2043

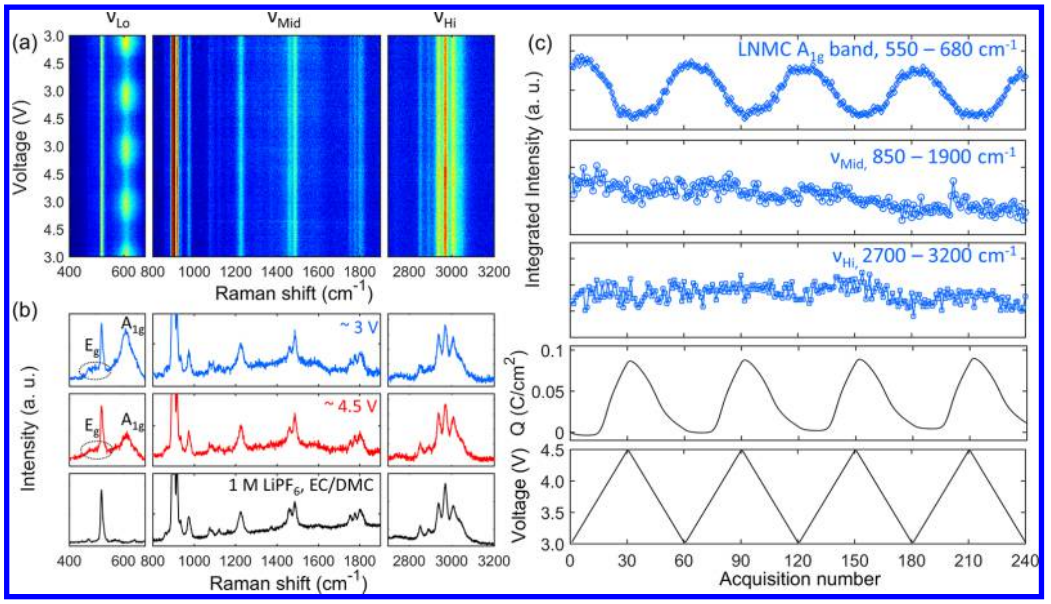

Figure 2. (a) Operando Raman spectral evolution acquired in four consecutive cycles for an LNMC electrode. The cell voltage was cycled between 3−4.5 V and each spectrum was acquired within a voltage interval of 50 mV. (b) Representative spectra acquired at the low voltage state (~3 V, blue) and the high voltage state (~4.5 V, red) in comparison with a Raman spectrum of a 1 M EC/DMC $LiPF_6$ electrolyte (black). Vibrational energies for both spectral evolution shown in (a) and representative spectra shown in (b) are separated to ν_{Lo}, ν_{Mid}, and ν_{Hi} regions. (c) Evolution of integrated intensities for LNMC A_{1g} band, ν_{Mid}, and ν_{Hi} regions, stored charge, and the cell voltage profile as a function of spectral acquisition number during the operando measurement.

controlled monolayer without agglomeration and stacking. The localized surface plasmon resonance (LSPR) profile of the monolayer assembly (Figure 1d) shows a strong distinction peak, which covers the photon wavelengths of Raman shifts with 633 nm laser excitation. Comparing to short-wavelength lasers (e.g., 458, 488, and 514 nm), a longer-wavelength laser (633 nm, used in this study) is more suited to the operando study because it could provide deeper probing depths into the electrolyte,[31] which could reveal more signal of the CEI, and avoid laser-induced decomposition of electrolytes and fluorescence excitation.[32]

As shown in Figure 1e, a gold monolayer was deposited on the surface of the model electrode. The Au nanocubes, well dispersed between LNMC particles without agglomeration, serve as the source of Raman enhancement for the CEI analyses. In the Raman spectrum of the LNMC electrode (Figure 1f), there are two characteristic bands: the band located at ~600 and 480 cm^{-1}, representing the A_{1g} and E_g vibration mode of the $R\bar{3}m$ lattice, respectively.[33,34] Since the features of the two bands evolve with state-of-charge (SOC) of the LNMC electrode,[35,36] the evolution of the LNMC bands can be directly correlated with the evolution of the CEI species. Prior to operando Raman analyses, the electrochemical properties of the LNMC model electrode were carefully investigated. Although no binder or other additives were used, the cyclic voltammogram of the electrode shows the characteristic electrochemical behavior of LNMC.[37] After 100 cycles, approximately ~70% of the initial capacity was retained (Supporting Information). Moreover, the application of an Au nanocube monolayer did not result in any significant changes in the CV profile (Figure 1g) and the impedance spectra (under OCV condition, Figure 1h), indicating that the Au nanocubes are redox-inactive under the electrochemical testing conditions. Additionally, the same CV measurement is performed for bare current collectors (with and without Au nanocube monolayer, Figure S10). Comparing to the redox current of LNMC, the CV current of the stainless steel current collector is negligible. Slight increase of anodic current was observed when the voltage was approaching 4.5 V (Figure S10b), indicating that slight electro-oxidation of the electrolyte exists in the high-voltage region. Meanwhile, the difference between the CV profiles of the current collectors with or without Au nanocube monolayer is almost negligible, which indicates that Au is mostly redox-inactive. This observation agrees with previously reported works in which Au was incorporated in Li-ion battery cathodes.[38]

Relying on the prepared model electrodes and their electrochemical properties, we subsequently performed operando Raman analyses using an operando cell,[39] which is capable of extensive battery cycling. Prior to operando SERS analyses, normal operando Raman spectroscopic measurements without the Au monolayer was performed, aiming to analyze the evolution of bulk LNMC and the response of the electrolyte as a function of electrode potential. Figure 2a shows the evolution of operando Raman spectra while cell voltages were linearly scanned between 3−4.5 V for four continuous cycles. Raman spectra measured at the most charged (4.5 V) and the most discharged (3 V) states are highlighted and are compared with a Raman spectrum of the 1 M EC/DMC $LiPF_6$ electrolyte used in this study. Raman spectra analyses are performed within three important wavenumber regions where all vibration modes of the LNMC and the electrolyte are located. Raman bands of LNMC (i.e., A_{1g} and E_g bands) are located within the low-wavenumber region (ν_{Lo}, 400−680 cm^{-1}) and Raman bands of the electrolyte are primarily located within the midwavenumber and high-wavenumber regions. The Midwavenumber region (ν_{Mid}, 850−1900 cm^{-1}) includes stretching modes of C—C, C═C, C—O, C═O, and P—F bonds and bending modes of C—H bonds. The Hi-wavenumber region (ν_{Hi}, 2700−3200 cm^{-1}) describes stretching vibration of C—H bonds. As the cell voltage was cycled periodically, as shown in Figure 2a, the intensity of the

DOI: 10.1021/acs.nanolett.9b00179
Nano Lett. 2019, 19, 2037−2043

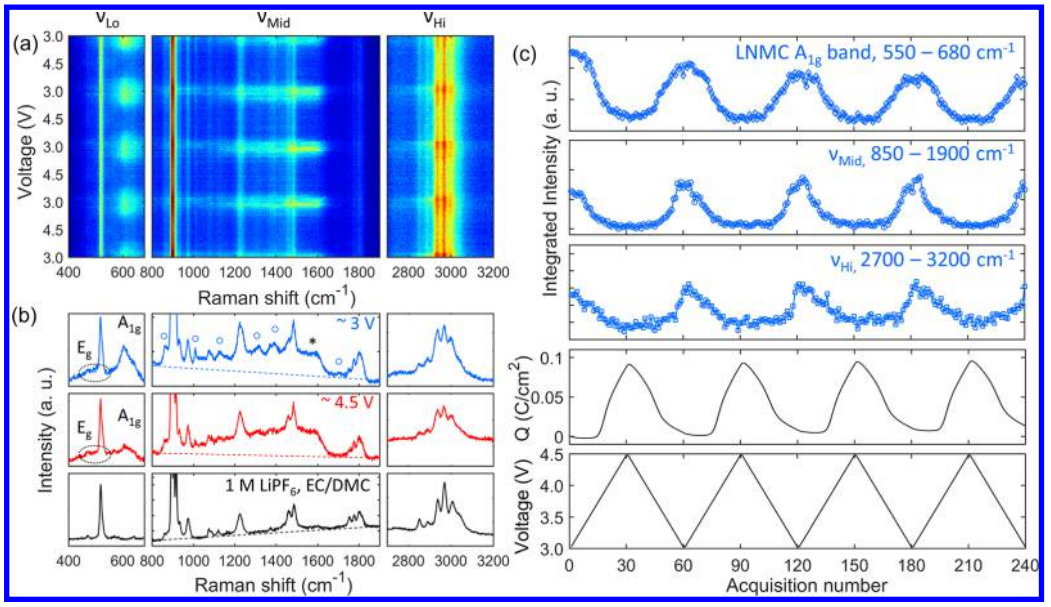

Figure 3. (a) Operando Raman spectral evolution acquired in four consecutive cycles for an LNMC electrode. Au nanocubes were deposited on the LNMC surface via Langmuir−Blodgett method prior to the operando test. The cell was cycled between 3−4.5 V and each spectrum is acquired within a voltage interval of 50 mV. (b) Representative spectra acquired at the low voltage state (~3 V, blue) and the high voltage state (~4.5 V, red) in comparison with a Raman spectrum of a 1 M EC/DMC $LiPF_6$ electrolyte (black). Raman bands related to CEI are marked with blue circles and the band likely contributed by oxidation of the electrolyte is marked with an asterisk. The baselines of the ν_{Mid} region are marked by dash lines. Vibrational energies for both spectral evolution shown in (a) and representative spectra shown in (b) are separated to ν_{Lo}, ν_{Mid}, and ν_{Hi} regions. (c) Evolution of integrated intensities for LNMC A_{1g} band, ν_{Mid}, and ν_{Hi} regions, stored charge, and the cell voltage profile as a function of spectral acquisition number during the operando measurement.

A_{1g} band decreases during the anodic process (3−4.5 V) and increases during the cathodic process (4.5−3 V). In contrast, the E_g band, which is weak in intensity and partially overlaps with a sharp electrolyte band, is mostly unchanged (marked by dash eclipses). Highlighted spectra acquired at the most oxidized state and reduced state (Figure 2b, ν_{Lo}) clearly demonstrate the effect of electrode potential on the vibrational modes of LNMC. Quantified intensity of the A_{1g} band (Figure 2c) shows an oscillation-like evolution. As the intensity of the E_g mode is weak and it overlaps with a sharp solvent band, the E_g mode was not tracked quantitatively. Interestingly, the oscillation-like evolution of the A_{1g} band is in an excellent negative correlation with the evolution of stored charge. The evolution of stored charge is obtained by integrating the CV current as a function of time (Figure S4). The A_{1g} band intensity minimized at the highest state-of-charge and reaches maximum values at lowest state-of-charge. Such strong correlation is because removal of interlayer cations from $R\bar{3}m$-structured layers (not limiting to LNMC) would systematically affect electronic structures of transition metal and oxygen and thus changes the polarizability of the A_{1g} and E_g modes,[35,36,40,41] leading to a quantitative correlation between $I(A_{1g})/I(E_g)$ and the state of charge.

In the ν_{Mid} and ν_{Hi} regions, Raman bands did not undergo any significant evolution throughout the entire operando test (Figure 2a). Thus, Raman spectra in both ν_{Mid} and ν_{Hi} regions acquired at 4.5 and 3 V are almost the same with those of the electrolyte, by exhibiting the identical positions and profiles for each Raman bands. The Raman bands of the electrolyte can be accurately assigned to bands of EC, DMC, PF_6^-, and solvation bands due to Li-solvent interaction (Supporting Information). Quantified intensity evolution in the ν_{Mid} and ν_{Hi} regions demonstrates no obvious dynamics as a function of cell voltage (Figure 2c). The static evolution of ν_{Mid} and ν_{Hi} regions, where vibration modes of organic compounds are located, indicate that the properties of the bulk electrolyte remain stable. Nevertheless, it also suggests that normal Raman spectroscopy is not able to reveal the CEI species because of insufficient sensitivity. The operando Raman measurement without surface enhancement, which demonstrates the dynamics of bulk LNMC and the bulk electrolyte, could serve as a basis for further operando SERS investigation.

With the Au nanocube monolayer applied to the LNMC electrode, we performed the same operando Raman measurement, aiming to investigate the CEI chemical species and their dynamics. Evolution of operando Raman spectra for four continuous cycles is shown in Figure 3a and the quantitative intensity of different regions (ν_{Lo}, ν_{Mid}, and ν_{Hi}) are summarized in Figure 3c. Spectra acquired at the most charged and discharge states are shown in Figure 3b. After the LNMC SERS measurement, the same operando SERS measurement on the current collector was performed for comparative purposes (Figures S11 and S12). For LNMC, the intensity of the A_{1g} band demonstrate oscillating decrease and increase during the anodic and cathodic processes, respectively. Also, the oscillation-like evolution is in a strong negative correlation with the evolution of stored charge (Figure 3c), which is same as the case when Au nanocubes were not applied (Figure 2a and 2c). Such similarity is expected because Au nanocubes will not influence the structural evolution of LNMC during charge/discharge, as demonstrated in Figure 1g,h. However, for the ν_{Mid} and the ν_{Hi} region (Figure 3a), the spectral evolution is dramatically different with the evolution when SERS was not used. As shown in Figure 3a, a number of additional bands appeared besides pristine electrolyte bands and their intensities are more pronounced at lower voltages. These additional bands were generated during the discharge process of the first cycle (Supporting Information). Comparing

DOI: 10.1021/acs.nanolett.9b00179
Nano Lett. 2019, 19, 2037−2043

to the spectrum of the electrolyte, highlighted spectra acquired at 3 and 4.5 V clearly demonstrate the new bands observed in the operando measurement (Figure 3b). Also, in the ν_{Mid} region, Raman bands between 800 and 1700 cm^{-1} show higher background intensity, comparing to the baseline (marked as dash lines) and Raman bands of the electrolyte in this region. By comparing to the operando SERS measurement of a current collector, spectral changes unrelated to LNMC can be distinguished. The Raman bands near 1577 cm^{-1} (marked as an asterisk) and the higher background intensity should be attributed to slight electrochemical oxidation of the electrolyte solvent (Figure S12). The Raman bands contributed by LNMC interfacial behavior are marked as blue circles in Figure 3b.

A few physiochemical processes are possibly responsible for the spectral changes. In general, simple adsorption of solvent molecules may lead to changes in band profiles,[18,42] but rarely generates new Raman bands, because it is unlikely to change the fundamental vibration modes. Thus, the observation of new Raman bands is due likely to the formation of new Raman-active vibration modes induced by formation of new species. These new bands can be assigned to ν(C—O—C) stretching vibration for ether and ester linkages, ν(C═O) stretching vibration for ester groups, and δ(C—H) bending vibration (Table S1). The assignment is based on the handbook by Lin-Vien et al.,[43] and more details regarding band assignments are provided in Supporting Information. Since surface enhancement only takes place when analytes are in close vicinity with the electrical field generated by SERS nanoparticles, these bands represent the chemical content of the CEI and prove that the CEI contains organic species with ether and ester functional groups. Moreover, a number of Raman bands of the electrolyte exist within 1600−1850 cm^{-1} and 2700−3200 cm^{-1}, which are characteristic regions for stretching vibration of ester groups and C—H bonds, respectively. Under operando conditions, these bands exhibited significant profile changes (i.e., relative intensities changes and peak widths, Figure 3b) compared to pristine Raman bands of the electrolyte in these regions. At lower potential, it should be noted that, not only are the Raman band intensities stronger, but also the difference in intensity distribution of the Raman bands became more pronounced (Figures S8 and S9) compared to the electrolyte bands. Such a difference suggests that these regions also contain Raman bands of CEI, which overlap with pristine electrolyte bands and lead to the profile changes. Analyses of the difference in spectral weight distribution (with careful baseline treatment and spectra normalization) unveil these new bands (Figures S8 and S9), which belong obviously to the stretching vibration of the C═O bonds in ester-groups and C—H bonds (Table S2), a further indication that the CEI contains aliphatic esters.

Regarding the intensities, these ether and ester bands (marked by circles) show significantly stronger intensities at 3 V than at 4.5 V. Quantified intensity evolution for ν_{Mid} and ν_{Hi} regions demonstrates obvious dynamics as a function of cell voltage (Figure 3c) in contrast to the static evolution of ν_{Mid} and ν_{Hi} without surface enhancement (Figure 2c). The main purpose of the intensity quantification in this study is not to determine the exact amount of the interfacial species, but to demonstrate an overall dynamic evolution of the interfacial process as a function of the cell voltage. Interestingly, dynamics of ν_{Mid} and ν_{Hi} intensities, which represent dynamics of ether/ester groups, are in concert with dynamics of LNMC A_{1g} band. Further statistical analyses on band intensity and charge storage in LNMC (Figure S14) indicate that the ν_{Mid} and ν_{Hi} regions (ester and ether features) are strongly correlated to LNMC A_{1g} band. Lower SOC (i.e., cell voltage) provides a more favorable condition for the CEI-bound ester/ether species. Moreover, as the CEI bands are located at characteristic positions, tracking the properties of these specific bands can offer more detailed analyses. For example, the changes in intensity of the Raman bands at 1009 cm^{-1} (i.e., ν(C—O—C) for ester groups), 1130 cm^{-1} (i.e., ν(C—O—C) for aliphatic ethers), and 1315 cm^{-1} (i.e., ν(C—O—C) for ester groups), and the bands in the range of 1650−1850 cm^{-1} (i.e., ν(C═O) for ester groups) can be quantified as well (Figure S13). Evolutions of these detailed bands are in good agreement with general evolution of ν_{Mid} and ν_{Hi} (Figure 3c). Identification of CEI chemistry and the unraveled dynamics serve as a basis for the hypothesis of CEI evolution mechanisms, which will be discussed in the next section. Following the spectral dynamic analyses of the LNMC electrode, evolution of operando SERS spectra of the current collector was evaluated (Figure S11). The SERS spectra evolution without LNMC mostly demonstrates random fluctuations. At the highest voltage (~4.5 V), obscure intensity maximums can be found for ν_{Mid} and ν_{Hi} regions due most likely to a thin layer composed of oxidation products of the solvents on Au surface, driven by a small oxidation current (from 3.8 to 4.5 V). In the SERS spectral evolution of LNMC (Figure 3c), this thin layer of oxidation products may also present on the Au surface although such intensity maximum is not evident. Most likely, the predominant spectral evolution of CEI of LNMC (oscillating behavior shown in Figure 3c) overwhelms the spectral evolution contributed by electrolyte oxidation. Similarly, in the CV profiles of LNMC, the anodic current due to slight oxidative solvent decomposition is not discernible either; the redox current of LNMC is much larger and overwhelms the current contribution by electrolyte decomposition at high voltage condition. Additionally, despite the dramatic spectral evolution of the CEI, Raman spectrum of the electrolyte after extensive cycling is identical with that of the fresh electrolyte. This observation suggests that the spectral dynamics shown in Figure 3 is controlled by CEI instead of the bulk electrolyte and the composition change of the bulk electrolyte after cycling should be very limited.

We further investigated the mechanisms of CEI dynamics, on the basis of experimental observations. The intensities of the CEI bands maximize at low voltages while the reduction of carbonate ester is unlikely in the potential range for cathode (i.e., 3−4.5 V). Also, the upper voltage limit (4.5 V) is within the stability window of the electrolyte solvents. Thus, we believe that a polymerization/oligomerization reaction (a rough schematic is shown in Figure 4a) is the reason for the ester and ether species observed by operando SERS. Initiated by the reduction of ester carbonates at the anode, small ester molecules (EC and DMC) undergo a series nucleophilic chain reaction steps[5,44,45] and form polymer/oligomer chains containing ester and ether groups (detailed mechanism is shown in Figure S17). Comparing to identifying the CEI species, understanding the CEI dynamics observed by operando SERS is much more important, because behavior of CEI during extensive battery charge/discharges is closely related to dynamics of Li-ion storage and cycling behavior of a battery. Regarding the mechanism of the CEI dynamics, we consider the most likely reason is that the adsorption between

DOI: 10.1021/acs.nanolett.9b00179
Nano Lett. 2019, 19, 2037−2043

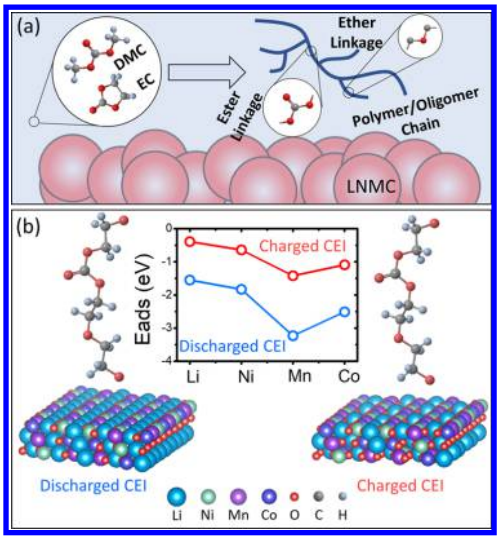

Figure 4. Modeling of CEI of LNMC. (a) Rough schematic of the chain reaction mechanism. Solvent molecules (EC and DMC) convert to polymer/oligomer chains with ether and ester linkages and get adsorbed on LNMC surface. (b) Demonstration of the model CEI used for ab initio calculations. The model CEI contains a (104) LNMC and a $L_{0.5}$NMC surface slab (for discharged and charged states, respectively) and a model chain molecule. The calculated adsorption energies of the model molecule on the LNMC and $L_{0.5}$NMC surfaces at different cation sites are compared.

polymer/oligomer chains and LNMC is more stable at lower voltages (i.e., lower SOC). On the other hand, the adsorption is not totally broken down at high SOC, as the CEI peaks are still clearly observed at high voltages. Statistically, the polymer/oligomer chains are more likely found at the interface at lower voltages, leading to the quantitative oscillation-like evolution. To fundamentally evaluate this hypothesis, we constructed a model CEI and analyzed the properties of the CEI at both discharged and charged conditions using ab initio calculations (Figure 4). For the LNMC in the model, based on previously reported crystallographic parameters,[46] we constructed a pristine LNMC unit cell to model the discharged state. The unit cell with half of Li removed (i.e., $L_{0.5}$NMC) after geometrical optimization was applied to model the charged state. Then, considering that (104) facet is one of the most stable surfaces for LNMC,[47,48] we applied the (104) surface slab to model the LNMC side for the CEI (Figure 4b). For the polymer/oligomer chain, we constructed a model molecule with a minimum chain length (Figure 4b) in accordance to the chain reaction mechanism (Figure S17). The interaction between the model molecule and the model LNMC surface is simulated as the adsorption of the oxygen (at the end of the chain) on one of the cation site (Li, Ni, Mn, and Co). The stability of the interfaces can be evaluated from the calculated adsorption energies. For both charged and discharged LNMC, the calculated adsorption energies for all sites are negative, indicating that the adsorption process is thermodynamically favorable for both charged and discharged states regardless of the cation sites. More importantly, the calculated adsorption energies for the charged interface ($L_{0.5}$NMC) are systematically higher than those of the discharged interface (LNMC), regardless of cation sites. Specifically, it appears that the adsorption is most stable at the Mn site and least stable at the Li site. The calculated trend is insensitive to calculation methodologies (i.e., DFT and DFT+U, Figure S19). Thus, based on the simple CEI model, the calculation results suggest that ester/ether chains tend to exist more within the CEI at the discharged state, which corroborates the experimental evolution of ester/ether bands shown in Figure 3c. Therefore, with the capability of operando SERS and the proposed CEI model, the hypothesized mechanism of CEI dynamics is validated.

In conclusion, we successfully investigated the CEI dynamics of a binder-free LNMC electrode using operando SERS. CEI species containing ester and ether chains were observed under operando condition owing to strong SERS effect provided by the Au nanocube monolayer. More importantly, during consecutive charge/discharge processes, Raman bands of CEI exhibited substantial dynamics, which is in precise accordance with evolution of LNMC bands. Subsequently, we constructed a model CEI in order to unravel the strong correlation between dynamics of CEI and SOC of LNMC. Further, DFT+U calculations suggest that adsorption of the model molecule on the model LNMC surface is more stable in the discharged state, which is consistent with the experimentally observed CEI dynamics. This study unravels the CEI for LNMC within the stability window of the electrolyte. Future work in this direction includes investigating the role of CEI on the electrochemical behavior of cathodes under various conditions, such as electron and ion transfer across the phase boundary of LNMC as a function of the areal density of adsorbed polymer/oligomer chains. Also, it is necessary to develop a reliable approach for producing a monolayer assembly with modified Au nanoparticles (e.g., Au−SiO_2) in order to explore their applications where Au is redox active (for example, in aqueous electrolytes). The methodology developed in this study can be applied to other energy-related fields to explore the nature of interfaces, which often governs the key redox reactions in energy storage/conversion systems.

■ ASSOCIATED CONTENT

Supporting Information

The Supporting Information is available free of charge on the ACS Publications website at DOI: 10.1021/acs.nanolett.9b00179.

Experimental Section, more electrochemical behavior of LNMC, more spectroscopic analyses, Raman band assignments, details of the CEI mechanism, the model CEI molecule, the model LNMC surface, and ab initio calculations (PDF)

■ AUTHOR INFORMATION

Corresponding Author

*E-mail: meilin.liu@mse.gatech.edu.

ORCID

Dongchang Chen: 0000-0002-2654-8176
Mahmoud A. Mahmoud: 0000-0002-1986-1797
Jeng-Han Wang: 0000-0002-3465-4067
Bote Zhao: 0000-0003-1236-6862
Meilin Liu: 0000-0002-6188-2372

Notes

The authors declare no competing financial interest.

DOI: 10.1021/acs.nanolett.9b00179
Nano Lett. 2019, 19, 2037−2043

■ ACKNOWLEDGMENTS

This work was supported by the U.S. National Science Foundation under award number DMR-1410320 and DMR-1742828.

■ REFERENCES

(1) Goodenough, J. B. *Acc. Chem. Res.* **2013**, *46*, 1053−1061.
(2) Goodenough, J. B.; Park, K.-S. *J. Am. Chem. Soc.* **2013**, *135*, 1167−1176.
(3) Armand, M.; Tarascon, J. M. *Nature* **2008**, *451*, 652.
(4) Xu, K. *Chem. Rev. (Washington, DC, U. S.)* **2014**, *114*, 11503−11618.
(5) Xu, K. *Chem. Rev. (Washington, DC, U. S.)* **2004**, *104*, 4303−4418.
(6) Aurbach, D.; Markovsky, B.; Salitra, G.; Markevich, E.; Talyossef, Y.; Koltypin, M.; Nazar, L.; Ellis, B.; Kovacheva, D. *J. Power Sources* **2007**, *165*, 491−499.
(7) Li, W.; Dolocan, A.; Oh, P.; Celio, H.; Park, S.; Cho, J.; Manthiram, A. *Nat. Commun.* **2017**, *8*, 14589.
(8) Kim, H.; Kim, M. G.; Jeong, H. Y.; Nam, H.; Cho, J. *Nano Lett.* **2015**, *15*, 2111−2119.
(9) Sun, Y.; Liu, N.; Cui, Y. *Nature Energy* **2016**, *1*, 16071.
(10) Hy, S.; Liu, H.; Zhang, M.; Qian, D.; Hwang, B.-J.; Meng, Y. S. *Energy Environ. Sci.* **2016**, *9*, 1931−1954.
(11) Goodenough, J. B.; Kim, Y. *Chem. Mater.* **2010**, *22*, 587−603.
(12) Maier, J. *Angew. Chem., Int. Ed.* **2013**, *52*, 4998−5026.
(13) Whittingham, M. S. *Chem. Rev. (Washington, DC, U. S.)* **2004**, *104*, 4271−4302.
(14) Ellis, B. L.; Lee, K. T.; Nazar, L. F. *Chem. Mater.* **2010**, *22*, 691−714.
(15) Carroll, K. J.; Qian, D.; Fell, C.; Calvin, S.; Veith, G. M.; Chi, M.; Baggetto, L.; Meng, Y. S. *Phys. Chem. Chem. Phys.* **2013**, *15*, 11128−11138.
(16) Tripathi, A. M.; Su, W.-N.; Hwang, B. J. *Chem. Soc. Rev.* **2018**, *47*, 736−851.
(17) Horowitz, Y.; Han, H.-L.; Ross, P. N.; Somorjai, G. A. *J. Am. Chem. Soc.* **2016**, *138*, 726−729.
(18) Yu, L.; Liu, H.; Wang, Y.; Kuwata, N.; Osawa, M.; Kawamura, J.; Ye, S. *Angew. Chem., Int. Ed.* **2013**, *52*, 5753−5756.
(19) Matsushita, T.; Dokko, K.; Kanamura, K. *J. Power Sources* **2005**, *146*, 360−364.
(20) Horowitz, Y.; Steinrück, H.-G.; Han, H.-L.; Cao, C.; Abate, I. I.; Tsao, Y.; Toney, M. F.; Somorjai, G. A. *Nano Lett.* **2018**, *18*, 2105−2111.
(21) Baddour-Hadjean, R.; Pereira-Ramos, J.-P. *Chem. Rev. (Washington, DC, U. S.)* **2010**, *110*, 1278−1319.
(22) Li, J.-F.; Zhang, Y.-J.; Ding, S.-Y.; Panneerselvam, R.; Tian, Z.-Q. *Chem. Rev. (Washington, DC, U. S.)* **2017**, *117*, 5002−5069.
(23) Cardinal, M. F.; Vander Ende, E.; Hackler, R. A.; McAnally, M. O.; Stair, P. C.; Schatz, G. C.; Van Duyne, R. P. *Chem. Soc. Rev.* **2017**, *46*, 3886.
(24) Peng, Z.; Freunberger, S. A.; Chen, Y.; Bruce, P. G. *Science* **2012**, *337*, 563−566.
(25) Hy, S.; Felix, F.; Rick, J.; Su, W.-N.; Hwang, B. J. *J. Am. Chem. Soc.* **2014**, *136*, 999−1007.
(26) Hu, R.; Chen, D.; Waller, G.; Ouyang, Y.; Chen, Y.; Zhao, B.; Rainwater, B.; Yang, C.; Zhu, M.; Liu, M. *Energy Environ. Sci.* **2016**, *9*, 595−603.
(27) Yin, S. C.; Rho, Y. H.; Swainson, I.; Nazar, L. F. *Chem. Mater.* **2006**, *18*, 1901−1910.
(28) Sisco, P. N.; Murphy, C. J. *J. Phys. Chem. A* **2009**, *113*, 3973−3978.
(29) Mahmoud, M. A. *J. Phys. Chem. C* **2015**, *119*, 305−314.
(30) Mahmoud, M. A. *J. Chem. Phys.* **2015**, *143*, 074703.
(31) Iwata, N.; Itoh, T. In *Development of In Situ Raman Technique for Li-Ion Battery*; 223rd ECS Meeting, Toronto, Ontario, Canada, May 12−17, 2013; ECS, 2013.
(32) Jarry, A.; Gottis, S.; Yu, Y.-S.; Roque-Rosell, J.; Kim, C.; Cabana, J.; Kerr, J.; Kostecki, R. *J. Am. Chem. Soc.* **2015**, *137*, 3533−3539.
(33) Ruther, R. E.; Callender, A. F.; Zhou, H.; Martha, S. K.; Nanda, J. *J. Electrochem. Soc.* **2015**, *162*, A98−A102.
(34) Inaba, M.; Iriyama, Y.; Ogumi, Z.; Todzuka, Y.; Tasaka, A. *J. Raman Spectrosc.* **1997**, *28*, 613−617.
(35) Lei, J.; McLarnon, F.; Kostecki, R. *J. Phys. Chem. B* **2005**, *109*, 952−957.
(36) Lanz, P.; Villevieille, C.; Novák, P. *Electrochim. Acta* **2014**, *130*, 206−212.
(37) Ohzuku, T.; Makimura, Y. *Chem. Lett.* **2001**, *30*, 642−643.
(38) Esbenshade, J. L.; Fox, M. D.; Gewirth, A. A. *J. Electrochem. Soc.* **2015**, *162*, A26−A29.
(39) Chen, D.; Wang, J.-H.; Chou, T.-F.; Zhao, B.; El-Sayed, M. A.; Liu, M. *J. Am. Chem. Soc.* **2017**, *139*, 7071−7081.
(40) Nanda, J.; Remillard, J.; O'Neill, A.; Bernardi, D.; Ro, T.; Nietering, K. E.; Go, J.-Y.; Miller, T. J. *Adv. Funct. Mater.* **2011**, *21*, 3282−3290.
(41) Chen, D.; Xiong, X.; Zhao, B.; Mahmoud, M. A.; El-Sayed, M. A.; Liu, M. *Advanced Science* **2016**, *3*, 1500433.
(42) Liu, H.; Tong, Y.; Kuwata, N.; Osawa, M.; Kawamura, J.; Ye, S. *J. Phys. Chem. C* **2009**, *113*, 20531−20534.
(43) Lin-vien, D.; B. Colthup, N.; G. Fateley, W.; G. Grasselli, J. *The Handbook of IR and Raman Characteristic Frequencies of Organic Molecules*; Academic Press: Cambridge, MA; 1991.
(44) Aurbach, D.; Levi, M. D.; Levi, E.; Teller, H.; Markovsky, B.; Salitra, G.; Heider, U.; Heider, L. *J. Electrochem. Soc.* **1998**, *145*, 3024−3034.
(45) Aurbach, D.; Gamolsky, K.; Markovsky, B.; Salitra, G.; Gofer, Y.; Heider, U.; Oesten, R.; Schmidt, M. *J. Electrochem. Soc.* **2000**, *147*, 1322−1331.
(46) Yabuuchi, N.; Koyama, Y.; Nakayama, N.; Ohzuku, T. *J. Electrochem. Soc.* **2005**, *152*, A1434−A1440.
(47) Garcia, J. C.; Bareño, J.; Yan, J.; Chen, G.; Hauser, A.; Croy, J. R.; Iddir, H. *J. Phys. Chem. C* **2017**, *121*, 8290−8299.
(48) Kramer, D.; Ceder, G. *Chem. Mater.* **2009**, *21*, 3799−3809.

DOI: 10.1021/acs.nanolett.9b00179
Nano Lett. 2019, 19, 2037−2043